

Calderoni Giovanna (Orcid ID: 0000-0002-3712-4432)
Di Giovambattista Rita (Orcid ID: 0000-0001-5622-1396)

Stress drop, apparent stress, and radiation efficiency of clustered earthquakes in the nucleation volume of the April 6, 2009, M_w 6.1 L'Aquila earthquake

Giovanna Calderoni, Antonio Rovelli, and Rita Di Giovambattista
Istituto Nazionale di Geofisica e Vulcanologia
Via di Vigna Murata 605
00143 Rome, Italy

Abstract

We investigate the variability of Brune stress drop ($\Delta\sigma$) and apparent stress (τ_a) of 23 earthquakes occurred in a small crustal volume adjacent to the hypocenter of the destructive M_w 6.1 L'Aquila earthquake. Their magnitude range is $2.7 \leq M_w \leq 4.1$. Inter-event variability of stress drop and apparent stress results in a factor of ten, well beyond the individual-event uncertainty. Radiation efficiency $\eta_{sw} = \tau_a/\Delta\sigma$ varies mostly between 0.1 and 0.2 but, in the days immediately before and after the main shock, η_{sw} tends to be smaller decreasing to values as low as 0.06. This may be the consequence of ruptures migrating in those days into a focal volume with higher dynamic strength. The temporal change of η_{sw} is tentatively interpreted as a spatial variation due to the earthquake migration into the locked portion of the fault that originated the main shock. Consistently, no variation in stress drop and apparent stress is observed between foreshocks and aftershocks but the smallest and largest $\Delta\sigma$ result in a good correlation with the largest and smallest b -values, respectively, imaged by other authors in the rupture nucleation volume.

This article has been accepted for publication and undergone full peer review but has not been through the copyediting, typesetting, pagination and proofreading process which may lead to differences between this version and the Version of Record. Please cite this article as doi: 10.1029/2019JB017513

1) Introduction

The 6 April 2009, M_w 6.1 L'Aquila earthquake was preceded by an intense foreshock activity that started around October 2008 and accelerated in the early 2009. The largest foreshock (M_w 4.1) occurred on 30 March, seven days before the main shock. After this event, seismic activity increased even more and changed significantly in terms of location, time of occurrence and magnitude [Di Luccio *et al.*, 2010]. Foreshocks preceding the March 30, M_w 4.1 earthquake were concentrated in the northern part of the nucleation zone whereas events following that foreshock migrated to the south (Fig. 1).

Concomitantly with the change of the spatial-temporal distribution of the events [Telesca, 2010] and the b -value [Papadopoulos *et al.*, 2010; Sukan *et al.*, 2014], the M_w 4.1 foreshock marked the beginning of an abrupt temporal change in other seismic parameters such as the P -to- S wave velocity ratio in the crust [Di Luccio *et al.*, 2010; Lucente *et al.*, 2010] and S -wave velocity in the damage fault zone [Calderoni *et al.*, 2015 a]. The latter paper provided a precise timing of the temporal variations in the source volume, indicating an abrupt change around a ten of hours after the M_w 4.1 foreshock. The significant velocity variation in the fault zone was well constrained in time by amplitude variations of fault-trapped waves and a concomitant loss of waveform coherence in a cluster of repeating earthquakes in the main shock nucleation volume.

The earthquakes used by Calderoni *et al.* [2015 a] have a spatial distribution that is optimal for an investigation of the state of stress in the nucleation volume. A study of repeating earthquakes yielded important results on the San Andreas Fault at Parkfield where Abercrombie [2014] found a sharp decrease of stress drop with the 2004, M_w 6 earthquake followed by a fast return to previous values. Goebel *et al.* [2015] and Goebel *et al.* [2017] detected significant regional variations of stress drop in Southern California, neatly beyond measurement uncertainties. Yoshida *et al.* [2017] observed well constrained temporal variations of stress drop in an earthquake swarm that started 7 days after the 2011 M_w 9.0 Tohoku-Oki earthquake beneath the caldera structure near the border between Yamagata and Fukushima Prefectures in NE Japan. Moreover, they found a significant anti-correlation with temporal variations of b -value.

In this study, we have enlarged the dataset of Calderoni *et al.* [2015 a] including as much as possible nearby earthquakes with the goal of seeking for temporal and/or spatial variation of stress parameters in the nucleation volume of the destructive M_w 6.1 L'Aquila earthquake. The attention is focused on earthquakes between the M_w 4.1 foreshock and the aftershocks that occurred immediately after the M_w 6.1 main shock. The major challenge of such a type of studies is the reliability of values estimated for stress parameters [Prieto *et al.*, 2006; Abercrombie, 2015]. Abercrombie [2015] provides very detailed suggestions on tests needed to avoid biased estimates and to check the real significance of inter-event variability. Based on many of its indications, the effort in this study is to estimate stress parameters in the preparatory phase of the M_w 6.1 L'Aquila earthquake and after the main shock, with a special attention to the small crustal volume between the main shock and the M_w 4.1 foreshock. In the same zone, Sukan *et al.* [2014] imaged a patch near the main shock nucleation point, characterized by a low b -value: a possible correlation between spatial variations of b -value and stress drop is also investigated in this study, zooming the analysis to a scale of few kilometers.

2) Data

The dataset of this study comprises 9 of the repeating earthquakes used by *Calderoni et al.* [2015 a]. These earthquakes are part of a cluster located a few kilometres to the southwest of the main shock nucleation point that were selected as having precise hypocentral determinations and moment magnitude available from independent moment tensor determinations. The dataset in analysis also includes 17 earthquakes located in a $2.5 \times 2.5 \times 2.5 \text{ km}^3$ crust volume (see Fig. 1) adjacent to those used by *Calderoni et al.* [2015 a]. The selection criterion for these earthquakes was based on a cross-correlation analysis of waveform similarity as already done by *Calderoni et al.* [2015 a]. The cross-correlation coefficients (CC) were computed using the vertical and horizontal components of station FIAM, orthogonal to the fault strike, after band-pass filtering of uncorrected data between 1 and 6 Hz. When records of FIAM were not available, stations VCEL or FAGN were alternatively used for the computation of CC. The procedure details are described in *Calderoni et al.* [2015 a]. The selected events resulted having CC to range between 0.7 and 0.96, they are listed in Table 1. This table includes: 23 target events, both foreshocks (from # 1 to #11) and aftershocks (from # 13 to #24), in a magnitude range $2.7 \leq M_w \leq 4.1$; the main shock (event # 12), its unclipped records were analyzed as well; 3 smaller magnitude earthquakes (from # 25 to #27), used for the EGF deconvolution of target events. Hypocenter determinations are from *Chiaraluce et al.* [2011], who used a double-difference algorithm. Seismic moments M_0 are taken from *Herrmann et al.* [2011] and when not available, as for some of the smallest events, the value of M_0 is determined through spectral scaling of the low-frequency displacement plateau using larger magnitude nearby events with known M_0 . Moment-magnitudes M_w are scaled from M_0 following *Hanks and Kanamori* [1979].

Seismograms are those recorded by the seismological stations (mostly 24-bit broadband 40-s Nanometrics Trillium) of the Italian Seismic Network run by the Istituto Nazionale di Geofisica e Vulcanologia (INGV). Density and azimuthal coverage of stations is illustrated in Fig. 1. Data were downloaded from the website (<http://iside.rm.ingv.it/iside/standard/index.jsp>). The instrumental correction was performed using the factory supplied zeroes and poles of seismometer transfer functions, the corrected velocity time series were used in the analysis. Data processing and spectral computations used the SAC software [*Goldstein et al.*, 2003].

For each of the selected events, the signal-to-noise ratio (SNR) was computed at the available stations. The signal duration of each seismogram is decided on the basis of the cumulative integral of squared velocity of the horizontal components, the time window of analysis starts with the direct S wave arrival and ends up to include the 95% of the asymptotic trend (Fig. 2). A noise segment having the same duration is extracted before the *P*-wave arrival. Both noise and signal windows are tapered with a 10% cosine box, then FFT is computed. Noise and signal spectra are averaged on the horizontal components (geometrical mean). The usable frequency bandwidth is determined for each seismogram by the ratio between signal and noise spectra that must be greater than a fixed threshold (usually 3 or 5 in the literature). The criterion adopted in this study is $\text{SNR} > 3$, we preferred the less restrictive value so as to increase the number of stations in each event. Fig. 2 (a and b) shows some examples of seismograms at different magnitudes and source distances, f_{\min} and f_{\max} are the lower and upper bound of the frequency range where the SNR curve exceeds the threshold of 3 (the horizontal line in

the panels a and b of Fig. 2). To avoid complications deriving from the high-frequency spectral fluctuations, the estimate of f_{max} uses a smoothed version of the SNR curve (visualized in grey around f_{max}).

The pattern of the usable bandwidth ($f_{min} - f_{max}$) resulting for the entire dataset is shown in Fig. 2c, where f_{min} and f_{max} of seismograms are represented as function of magnitude and distance for the entire dataset. The usable bandwidth is 0.2-20 Hz for the largest part of the cluster, up to distances of a hundred kilometers, only for the smallest magnitude events a more limited frequency range (1-10 Hz, approximately) is found at large distances. As expected, the SNR of the main shock seismograms indicates an even larger usable bandwidth, especially at low frequency where many stations exceed 3 at the lowest used frequency of 0.05 Hz.

3) Method of Analysis

The amplitude spectrum of ground motion at distance R from the source is the convolution of the source, crustal wave propagation, and site contributions

$$V(f, R) = \Omega_0(f) \cdot (2\pi f) \cdot A(f, R) \cdot H(f)$$

(1)

where $V(f, R)$ is velocity and f is frequency, $A(f, R)$ accounts for the seismic wave attenuation along the source-to-station propagation path, and $H(f)$ is a site term accounting for near-surface propagation effects beneath the station. The source-radiated displacement spectrum is expressed as

$$\Omega_0(f) = \frac{F_s R_{\theta, \phi}}{4\pi\rho\beta^3} \frac{M_0}{1 + (f/f_0)^2}$$

(2)

where M_0 and f_0 are seismic moment and corner frequency, respectively [Brune, 1970 and 1971]. F_s accounts for the free-surface effect, taken equal to 2. $R_{\theta, \phi}$ is the radiation pattern, which represents the average S -wave radiation pattern over azimuth and take-off angles, it is taken equal to 0.55 according to Boore and Boatwright [1984]. For density (ρ) and shear-wave velocity in the source volume (β), the values 2.8 g/cm³ and 3.1 km/s were respectively used according to Herrmann *et al.* [2011].

Following Eshelby [1957] and Keilis-Borok [1959], the radius r and uniform stress drop $\Delta\sigma$ of a circular crack in an infinite Poisson solid are linked to M_0 and f_0 through the equations:

$$\Delta\sigma = \frac{7}{16} \frac{M_0}{r^3} \quad (3)$$

$$r = \frac{2.34\beta}{2\pi f_0} \quad (4)$$

In this study we estimate Brune stress drops in a conventional Empirical Green's Function (EGF) approach in the frequency domain. The amplitude Fourier spectrum of each of the earthquakes under analysis is divided by several EGFs recorded at the same site. *Abercrombie* [2015] demonstrated that a high number of EGFs is necessary to get a reliable estimate of source parameters. Moreover, the EGF magnitude should be sufficiently smaller than the one of the target event to get a clear separation between the numerator and denominator spectra, and the distance between EGF and target event should be no larger than the size of the target event source to prevent destructive interference that could decrease their spectral ratio amplitude [*Abercrombie*, 2015]. We have found three events (EGF1, EGF2, and EGF3 in Table 1) that obey as much as possible the magnitude and distance constraints. All are aftershocks, with a distance from the target event of 2 to 3 km. EGF1 and EGF2 occurred about 18 and 24 hours, respectively, after the main shock, and EGF3 one month later. Unfortunately, no EGF was found among foreshocks.

For all of the events under analysis, the velocity spectra of target and EGF events were computed using a fixed time window of 10 s bracketing the entire *S*-wave train and early coda. An equal duration ensures the same propagation effect in the numerator and denominator of the spectral ratio, and 10 s minimize the role of noise in the EGFs compared to longer durations. Only stations with SNR > 3 in the frequency band 1-10 Hz were used in the EGF deconvolutions. Before computing the spectral ratio, numerator and denominator were smoothed with a 0.2-Hz wide triangular operator.

The spectral ratio between target and EGF events eliminates propagation and site terms according to Equations 1 and 2, and gives the ratio of the source terms

$$\frac{V_1(f)}{V_2(f)} = \frac{M_{01}}{M_{02}} \cdot \frac{1 + (f / f_{02})^2}{1 + (f / f_{01})^2} \quad (5)$$

where M_{01} and f_{01} are seismic moment and corner frequency of the target event, and M_{02} and f_{02} are the same parameters of the EGF. The corner frequencies f_{01} and f_{02} are written in terms of seismic moment and stress drop through Equations 3 and 4, and the best-fit value of $\Delta\sigma_1$ is then estimated through a grid search procedure, after an independent computation of $\Delta\sigma_2$. As discussed in *Abercrombie* [2014], the corner frequency of the EGFs is typically sufficiently larger than the one of the target events to not affect the fit in terms of f_{01} and $\Delta\sigma_1$. We estimated $\Delta\sigma_2$ before the fit of $\Delta\sigma_1$ through Equation 5 where the source parameters of one (# 17) of the events analyzed in a

previous paper [Calderoni *et al.*, 2013] was used as reference in the spectral ratio. The values of f_{02} resulted to be in a 10% range around the upper bound of the usable bandwidth. *A posteriori*, the validity of the adopted procedure is confirmed by a difference of about 10% between the final estimate of event # 17 obtained in this study and the one taken from Calderoni *et al.* [2013].

For each station and each EGF, the quality of the fit is checked through the range in which the variance of the fit is within 5% of the minimum value (Fig. 3a). According to Abercrombie [2015], the width of the 5% range is used as estimate error of the fit. The final stress drop of each event is computed as the average over stations and over EGFs applying an inverse-error weighting. Specifically, we have applied Equation 2 of Abercrombie [2015] for the computation of average and standard deviation of stress drop. The values of $\Delta\sigma_1$ derived for each event from different EGFs show differences of less than 0.2 in the log-scale (Fig. 3b). The small difference of stress drops estimated for different EGFs is important because confirms a uniformity of estimate uncertainty among events independently of magnitude and target-to-EGF distance.

As far as apparent stress τ_a is concerned, we followed the standard method of Wyss and Brune [1968] using the definition

$$\tau_a = \mu \frac{E_s}{M_0} \quad (6)$$

where μ is the crustal shear modulus set to 33 GPa and E_s is the radiated seismic energy. According to Singh and Ordaz [1994], we computed E_s as

$$E_s = \frac{4\pi\rho\beta}{F^2 R_{\theta,\varphi}^2} \int_{f_{min}}^{f_{max}} V^2(f) df \quad (7)$$

As described above, the cumulative integral of squared velocity was computed in the usable frequency bandwidth where the SNR is > 3 . The bandwidth limitation below f_{min} and above f_{max} is compensated according to the Di Bona and Rovelli [1988] approach. When the usable bandwidth is limited, the theoretical compensation can be larger than the integral computed with the real data: in this case the station is not used in the average. The final values of $V^2(f)$ were corrected for propagation and site effects, as prescribed by Equation 1. Details are discussed in the Appendix 1 as well as tests performed to assess the quality of results and variance reduction after propagation and site correction.

Finally, the radiation efficiency η_{sw} is computed through the ratio between apparent stress and static stress drop

$$\eta_{sw} = \tau_a / \Delta\sigma \quad (8)$$

This parameter, first introduced by Savage and Wood [1971], is the percentage of energy associated with the stress drop that is radiated [Beeler *et al.*, 2003]. According to

Beeler *et al.* [2012], for a pure omega-square model the value expected for η_{sw} is 0.23. Beeler *et al.* [2012] classified as high and low efficiency earthquakes those with $\eta_{sw} > 0.5$ and $\eta_{sw} < 0.1$, respectively. This parameter is a measure of the material dynamic strength: in studies concerning limited crustal volumes, it provides important hints on spatial and temporal changes of strength during earthquakes on preexisting faults [Wong, 1986; Kocharyan, 2013].

4) Results

The values of $\Delta\sigma$ resulting from the analysis vary from 0.1 to 2 MPa for the smaller events whereas $\Delta\sigma$ attains 8.7 MPa for the main shock (Fig. 4a). These estimates are consistent with those by other authors [Malagnini *et al.*, 2011; Calderoni *et al.*, 2013, Pačor *et al.*, 2016]. Fig. 4a suggests an increase of inter-event variability in the cluster toward the smallest magnitudes. This effect was already observed by Calderoni *et al.* [2013] after the analysis of a larger dataset representative of the entire structure activated during the L'Aquila seismic sequence. Rovelli and Calderoni [2016] confirmed the same behavior in other normal faulting earthquakes of the Apennines, in the Umbria-Marche region. In these papers, the increasing variability of stress drop at small magnitudes was interpreted as an effect of the higher sensitivity of smaller size ruptures to stress and strength heterogeneities in the focal volume. During the earthquake, the rupture propagation is controlled by a highly heterogeneous stress field [Ben-Zion and Zhu, 2002], and the amount of slip varies with the degree of heterogeneity [Fisher *et al.*, 1997; Ben-Zion, 2008]. The resulting stress drop, which is proportional to the ratio between slip and the rupture size, can vary much more when the rupture occurs in a small volume depending on the very local strength.

In Fig. 4a, we see that the stress drop variability at similar magnitudes is large and has the same extent for foreshocks and aftershocks. Events with $M_w < 3.2$ exhibit a stress drop that varies by one order of magnitude, and errors of individual events are much smaller than the inter-event variations. The neat separation of high frequency spectra for similar magnitude earthquakes, beyond the ± 1 standard deviation band of the station spectra, confirms the significance of the estimated stress drop difference in the cluster (Fig. 4, c and d).

Fig. 4b shows that apparent stress is well correlated with stress drop, and the ratio $\tau_a/\Delta\sigma$ is mostly comprised between 0.1 and 0.23, that is the range corresponding to the expectation of the omega-square model. However, there are also some events for which η_{sw} is lower, between 0.06 and 0.1: these low-efficiency values are typical of ruptures in crust volumes with higher dynamic strength.

Fig. 5 shows the temporal evolution of Brune stress drop, apparent stress and seismic efficiency during the entire period. The two stress parameters depict a similarly scattered trend, with the highest value corresponding to the main shock. Seismic efficiency is substantially stable versus time, however we can see that the events with the smallest values of η_{sw} are mostly concentrated in the days immediately before and after the main shock. Between April 5 and 6, η_{sw} has an average value of 0.08 whereas the average over the remaining earthquakes is 0.11, with a not significant overlap of the ± 1 standard deviation range about the average (0.09-0.14 for the former and 0.06-0.10 for the latter). A possible interpretation of this behavior is that η_{sw} of earthquakes migrating into the preparatory volume decreases to minimum values.

Interestingly, no significant variation in stress drop is observed between earthquakes preceding and following the main shock. The issue of possible variations between foreshocks and aftershocks has been debated for decades (e.g. *Tsujiura* [1977], *Zuñiga et al.* [1987], *Mori and Frankel* [1990], *Gibowicz* [2004], *Uchide et al.* [2014], to quote only a few among many). Often foreshocks have higher stress drop than aftershocks. However, this is not a rule, and differences in stress drop are more often ascribed to spatial variations of strength in the seismogenic volume independently of magnitude and regardless of the foreshock or aftershock group. Here, average stress drop and average apparent stress of foreshocks match fairly well the ones of aftershocks, as shown in Fig. 5.

5) Discussion

We estimated Brune stress drop based on the assumption of instantaneous rupture over a circular fault, as written above. When this assumption does not apply, like for extended faults with consequent rupture directivity, azimuthal variations of seismogram amplitudes affect individual-station estimates of stress parameters (e.g. *Calderoni et al.* [2013], *Abercrombie* [2015]). The 2009 L'Aquila seismic sequence was characterized by persistence of along-strike rupture directivity, even at small magnitudes [*Calderoni et al.*, 2015 b]. Therefore, the implications of the Brune model assumption have to be critically checked for our dataset. The effects of directivity on stress drop, apparent stress and radiation efficiency are evaluated looking at the pattern of individual-station values at different azimuths.

A neat difference emerges in the behavior of various events, three different examples are in Fig. 6. Azimuthal variations have a more evident extent for some events that show a systematical trend versus azimuth: this is the case of events # 9 and 18, indicating unilateral directivity in the rupture process. The azimuthal effects are particularly accentuated in the Brune stress drop: the physical explanation is the strong dependence of this parameter on the source pulse duration to the third power of corner frequency ($\Delta\sigma \approx f_c^3$). A dependence on directivity would be expected for apparent stress as well. However, in the integral of the squared velocity spectra of Equation 7, the increase of amplitude is partially compensated by a decrease of duration, and the resulting azimuthal effect due to directivity is less evident being masked in the estimate fluctuations. Moreover, the integral is made over the entire frequency band whereas directivity affects only frequencies above the corner frequency (e.g. see Fig.2 of *Calderoni et al.* [2017]). Fig. 6 shows that, when a systematic trend is observed, the azimuth of the largest values of Brune stress drop corresponds to the fault strike but can be reversed (to the northwest like in panel a or to the southeast like in panel b), indicating along-fault ruptures that propagate unilaterally to opposite directions in the two cases. This observation is consistent with results by *Calderoni et al.* [2015 b], who observed the persistence of along-strike rupture directivity in that portion of the L'Aquila fault. We can see that the difference in $\Delta\sigma$ between opposite along-fault directions can attain a factor of ten during unilateral ruptures, a result that is consistent with the *Kaneko and Shearer* [2015] conclusions. Since the systematic azimuthal variation in τ_a is smaller than in $\Delta\sigma$, the bias is not eliminated in the ratio of Equation 8 and estimates of η_{sw} maintain the dependence on azimuth, even though to a smaller extent compared to $\Delta\sigma$. The third example of Fig. 6 (event # 8) illustrates the case of an

earthquake with small (or no) directivity, characterized by parameter fluctuations that are smaller and not systematic in azimuth. Comparing the different events, we find that the effect of rupture directivity on η_{sw} results in a significant increase of inter-station variability with respect to circular (no directivity) ruptures.

After these tests we conclude that there is a neat evidence of rupture directivity in individual-station estimates of $\Delta\sigma$ and η_{sw} , much less in τ_a . However, since the spectra maintain the Brune-style shape, the model is applicable and the average over many azimuth and takeoff angles reduces the bias to an acceptable value. In fact, the amplitude variation in the forward direction is larger than in the backward direction, and the average of the directivity effect over azimuth is close to but not zero (see *Spudich and Chiou* [2008] and *Rowshandel* [2010]). However, the resulting bias is negligible compared to random estimate fluctuations.

Other tests were necessary to quantify the role that variability of crust properties plays on stress parameters. In Equations 2 to 4, density (ρ) and shear-velocity (β) are assumed to be constant but we know that several observations preceding the preparatory phase of the L'Aquila earthquake contradict this assumption. This implies that also rigidity (μ) changed during the time interval spanned by the investigated seismic events. Variations of β are particularly important because this parameter affects seismic wave amplitudes to the third power. Through the travel times of the closest stations around L'Aquila, *Lucente et al.* [2010] assessed a 5% decrease of β in and around the nucleation volume. The transient anomaly started one week before the main shock and ended with it. This time window corresponds to the interval 89 to 96 in terms of Julian day in Fig. 4. We note that the variation of stress drop is by more than a factor of 10 in the cluster within this time interval (Fig. 4). To ascribe the observed $\Delta\sigma$ variation entirely to the transient anomaly of shear velocity, the decrease of β should have been by a factor of 2 in the crust, that contrasts with all the available estimates of the L'Aquila earthquake [*Zaccarelli et al.*, 2011, *Di Luccio et al.*, 2010, *Lucente et al.*, 2010] and worldwide findings (e.g., see *Peng and Ben-Zion* [2006]). However, a change of β up to 5% would produce a bias smaller than 20% on $\Delta\sigma$, a variation that is within the measured error bars.

Also the possible effect of the medium variations on $A(f,R)$ and $H(f)$ was checked. Changes of the quality factor Q can be large ($> 10\%$) in concomitance with much smaller changes of β (e.g., see *Wang and Ma* [2015]). Moreover, the closest stations can also be sensitive to variations in elastic and inelastic properties of the upper layers [*Peng and Ben-Zion*, 2006; *Chao and Peng*, 2009] that likely change the site response $H(f)$. The propagation and site terms used in the Appendix 1 to estimate source parameters are an average over about 6 months, but variations of $A(f,R)$ and $H(f)$ are expected in the preparatory phase especially for the closest ($R < 40$ km) stations. To check if the bias due to changes in the shallow crust could be significant, we have repeated the stress drop estimate using only stations at distances larger than 40 km, that are less affected by variations in the preparatory volume. The use of a smaller number of stations increased the estimate uncertainties but the average values differed by less than 5% from the log values resulting from the entire distance range. This result suggests that perturbations in the crust near the source have a limited effect on stress estimates, within the estimate uncertainty.

A final issue that is faced in this study is the inverse relationship between stress drop and b -value (e.g. *Smith and Priestley* [2000], *Ruhl et al.* [2017]), to a scale of few kilometers. We have analyzed the spatial distribution of the cluster events from this

perspective. As done in Fig. 4, foreshocks and aftershocks are represented in Fig. 7 with different symbols and stress drop values are varied with the same color scale from blue to red. Fig. 7 shows that the high stress drop events spread around the largest M_w 4.1 foreshock, south to southeast of the main shock, whereas the lower stress drop events tend to be concentrated to the south at a larger distance from the main shock. The occurrence of a spatial variation in the main shock nucleation zone was also proposed by *Sugan et al.* [2014] that found significantly lower b -values in a patch of about 4 km² adjacent to the main shock nucleation. We have checked if a correlation exists between the highest stress drop events and the lowest b -value anomaly. If we superimpose the cluster of the present study over the area with the b -value variations (Fig. 7), we observe that the cluster distributes within two of the four zones imaged by *Sugan et al.* [2014], namely zones S2 and S3. The former corresponds to the lowest b -value anomaly (0.79, on average), very close to the main shock hypocenter, represented in blue as in *Sugan et al.* [2014], and the latter zone (in pink) is south of the previous one with a higher b -value (0.95, on average). Out of the 16 events that fall in zone S2, 14 have stress drops of the order or greater than 1 MPa (colors in the tones of red) and only 2 have a lower stress drop (colors in the tones of blue). Even better, all the events that fall in zone S3 have stress drops lower by more than a factor of 2 compared to zone S2, which is beyond the error uncertainty. According to *Sugan et al.* [2014], the lowest b -value anomaly represents a highly stressed patch of the fault ruptured by the main shock, and consistently many of the highest stress drop events are found to occur inside that patch. Therefore, also the temporal change of η_{sw} discussed in the previous section can be seen as a spatial effect due the seismicity migration into the crustal volume where the main shock nucleated.

6) Concluding remarks

We analyzed Brune stress drop, apparent stress, and radiation efficiency of 23 earthquakes ($2.7 \leq M_w \leq 4.1$) occurring in a small crustal volume adjacent to the hypocenter of the 6 April 2009, M_w 6.1 L'Aquila earthquake. The earthquake cluster spreads in time from February to July 2009 and contains both foreshocks and aftershocks. Although the dataset is limited in number, the application of the EGF technique to highly correlated waveforms of target events and EGFs allowed us to resolve statistically significant variations in earthquake stress drop that reflect quite well the different high frequency source radiation of events. Although the effect of source directivity can be very important for individual-station estimates even at small magnitudes, the average over many stations reduces the bias within random estimate fluctuations. The analysis of clustered earthquakes in a small volume leads to a finer spatial resolution than previous studies on the source parameters of the 2009 seismic sequence. No difference is found in the stress parameters between foreshocks and aftershocks in the cluster. Our results suggest that stress drop variations are originated by an asperity patch, and a good correlation is found at the scale of a few kilometers between the smallest and largest $\Delta\sigma$ with the largest and smallest b -values, respectively, found by other authors. The ratio between Brune stress drop and apparent stress (the radiation efficiency) ranges mostly between 0.1 and 0.15. However, in the days immediately before and after the main shock, radiation efficiency decreases below 0.1, down to values as low as 0.06, consistently with ruptures that propagate into the focal volume with the highest dynamic strength.

Acknowledgments. Some of the figures were created using GMT [Wessel and Smith, 1991]. Seismic Analysis Code (SAC) [Goldstein *et al.*, 2003] was used for much of the analysis. Data from the DPC can be downloaded from the Italian ACcelerometric Archive (ITACA) (<http://itaca.mi.ingv.it>), while data from the INGV are accessible from the European Integrated Data Archive (EIDA) (<http://eida.rm.ingv.it/>) and from the Italian Seismological Instrumental and Parametric Data-Base (ISIDe) (<http://iside.rm.ingv.it/>). We benefited from many conversations with Rachel Abercrombie. Many thanks are due to the Editor, Yehuda Ben-Zion, and two anonymous reviewers for their critical comments and constructive suggestions.

Appendix 1

To estimate the source radiated energy of the cluster events, the velocity squared spectrum computed from seismogram is corrected for long-path propagation and site terms ($A(f, R)$ and $H(f)$, respectively), according to Equation 1 of the text. Two different methods were checked (those by *Calderoni et al.* [2013] and *Pacor et al.* [2016]), and the one allowing the minimum variance was adopted. The smallest dispersion of source radiated spectra was obtained with the former one. In that approach, the propagation term is written as

$$A(f, R) = G(R) \exp(-\pi\kappa f) \quad (A1)$$

where $G(R)$ is the geometrical spreading, that is assumed to be spherical ($1/R$), and the exponential term represents the attenuation of seismic waves in the crust along the entire source-to-station path S . The parameter κ

$$\kappa = \int \frac{1}{Q} ds \quad (A2)$$

accounts for the earth quality factor Q [Anderson and Hough, 1984] and varies station by station. It is assumed not to depend on magnitude. For many of the seismological stations run in the region during the 2009 L'Aquila seismic sequence, this parameter was already computed by *Calderoni et al.* [2013] as an average over the ensemble of the $M_w > 5$ earthquakes. We have extended the analysis to further stations used in the present study. The final results are shown in Figure A1. Due to the structure of Equation A2 there is a trend of κ to increase with source distance but the variability at similar distances can be large because of variations of Q in the uppermost layers at different stations.

To estimate the site terms $H(f)$, the velocity spectra computed from seismograms are scaled to unitary distance through $1/R$ and compensated at high frequency through $\exp(\pi\kappa f)$. Therefore, for each event, the scaled spectra of available stations are averaged and the difference from the mean event spectrum is computed for each station. These

differences are averaged over the event ensemble thus obtaining a mean curve $H(f)$ for each station, with its ± 1 s. d. uncertainty about the geometric mean. Figure A2 shows two representative examples, for stations with large and small site amplification. Figure A3 shows to what extent the application of site correction decreases the dispersion of the source radiated spectra.

After the correction of both $A(f,R)$ and $H(f)$, we have checked the improvement of dispersion in the estimated source spectra and the lack of bias. In Figure A4 we can see the resulting source spectra of stations available for example events, drawn separately for stations at close ($R < 60$ km, in red) and large distance ($R > 60$ km, in black). If we consider the statistical deviation of individual-station spectra from the theoretical source model (green curve in Fig. A4), we find that the sample population of stations with $R < 60$ km shows a histogram of quadratic deviations from the theoretical model that matches strictly the histogram of stations with $R > 60$ km. This is a satisfactory indication that no bias versus distance is produced by the propagation and site correction.

REFERENCES

Abercrombie, R. E. (2014). Stress drops of repeating earthquakes on the San Andreas Fault at Parkfield, *Geophys. Res. Lett.*, 41, 8784–8791, doi:10.1002/2014GL062079.

Abercrombie, R. E. (2015). Investigating uncertainties in empirical Green's function analysis of earthquake source parameter, *J. Geophys. Res. Solid Earth*, 120, 4263–4277, doi:10.1002/2015JB011984.

Anderson, J.G. and S. E. Hough (1984). A model for the shape of the Fourier amplitude spectrum of acceleration at high frequencies, *Bull. seism. Soc. Am.*, 74, 1969–1993.

Beeler, N. M., T.-F. Wong, and S. H. Hickman (2003). On the expected relationships among apparent stress, static stress drop, effective shear fracture energy, and efficiency, *Bull. seism. Soc. Am.*, 93, 1381–1389.

Beeler, N. M., B. Kilgore, A. McGarr, J. Fletcher, J. Evans, and S. R. Baker (2012). Observed source parameters for dynamic rupture with non-uniform initial stress and relatively high fracture energy, *Journal of Structural Geology*, 38, 77–89.

Ben-Zion, Y. (2008). Collective behavior of earthquakes and faults: continuum-discrete transitions, evolutionary changes and corresponding dynamic regimes, *Rev. Geophys.*, 46, RG4006, doi:10.1029/2008RG000260.

Ben-Zion, Y. and L. Zhu (2002). Potency-magnitude scaling relations for Southern California earthquakes with $1.0 < M_L < 7.0$, *Geophys. J. Int.*, 148, F1–F5.

Boore, D. M. and J. Boatwright (1984). Average body-wave radiation coefficients, *Bull. seism. Soc. Am.*, 74, 1615–1621.

Brune, J. N. (1970). Tectonic stress and the spectra of seismic shear waves from earthquakes, *J. Geophys. Res.*, 75, 4997–5009.

Brune, J. N. (1971). Correction (to Brune 1970), *J. geophys. Res.*, 76, 5002.

Calderoni, G., A. Rovelli, and S. K. Singh (2013). Stress drop and source scaling of the 2009 April L'Aquila earthquakes, *Geophys. J. Int.*, 192, 260–264.

Calderoni, G., A. Rovelli, and R. Di Giovambattista (2015 a). Transient anomaly in fault zone-trapped waves during the preparatory phase of the 6 April 2009, Mw 6.3 L'Aquila earthquake, *Geophys. Res. Lett.*, 42, doi:10.1002/2015GL063176.

Calderoni, G., A. Rovelli, Y. Ben-Zion, and R. Di Giovambattista (2015 b). Along-strike rupture directivity of earthquakes of the 2009 L'Aquila, central Italy, seismic sequence, *Geophys. J. Int.*, 203, 399–415, doi.org/10.1093/gji/ggv275.

Calderoni, G., A. Rovelli, and R. Di Giovambattista (2017). Rupture directivity of the strongest 2016–2017 central Italy earthquakes. *J. Geophys. Res., Solid Earth*, 122, doi.org/10.1002/2017JB014118.

Chao, K. and Z. Peng (2009). Temporal changes of seismic velocity and anisotropy in the shallow crust induced by the 1999 October 22 M6.4 Chia-Yi, Taiwan earthquake, *Geophys. J. Int.*, 179, 1800–1816, doi:10.1111/j.1365-246X.2009.04384.x

Di Bona, M., and A. Rovelli (1988). Effects of the bandwidth limitation on stress drops estimated from integral of the ground motion, *Bull. Seismol. Soc. Am.*, 78, 1818–1825.

Di Luccio, F., G. Ventura, R. Di Giovambattista, A. Piscini, and F. R. Cinti (2010). Normal faults and thrusts reactivated by deep fluids: The 6 April 2009 Mw 6.3 L'Aquila earthquake, central Italy, *J. Geophys. Res. Solid Earth*, 115, B06315, doi:10.1029/2009JB007190.

DISS Working Group (2010). Database of Individual Seismogenic Sources (DISS), Version 3.1.1: A compilation of potential sources for earthquakes larger than M 5.5 in Italy and surrounding areas, <http://diss.rm.ingv.it/diss/>, © INGV 2010 - Istituto Nazionale di Geofisica e Vulcanologia, Rome, Italy.

Eshelby, J. (1957). The elastic field of an ellipsoid inclusion and related problems, *Proc. R. Soc. Lond.*, 241(1226), 376–396.

Fisher, D.S., K. Dahmen, S. Ramanathan, and Y. Ben-Zion (1997). Statistics of earthquakes in simple models of heterogeneous faults, *Phys. Rev. Lett.*, 78, 4885–4888.

Gibowicz, S. J. (2004). Stress release during earthquake sequences, *Acta Geophysica Polonica*, 52(3), 271–299.

Goebel, T. H. W. E. Hauksson, P. M. Shearer, and J.-P. Ampuero (2015). Stress-drop heterogeneity within tectonically complex regions: A case study of San Geronimo Pass, Southern California, *Geophys. J. Int.*, 202, 514–528, doi:10.1093/gji/ggv160.

Goebel, T. H. W. E. Hauksson, A. Plesh, and J. H. Shaw (2017). Detecting significant stress drop variations in large micro-earthquake datasets: a comparison between a convergent step-over in the San Andreas Fault and the Ventura thrust fault system, Southern California, *Pure Appl. Geophys.* 174, 2311–2330, doi:10.1007/s00024-016-1326-8.

Goldstein, P., D. Dodge, M. Firpo, and L. Minner (2003). SAC2000: signal processing and analysis tools for seismologists and engineers, in *Invited Contribution to 'The IASPEI International Handbook of Earthquake and Engineering Seismology'*, Eds W. H. K. Lee, H. Kanamori, P. C. Jennings and C. Kisslinger, Academic Press, London.

Hanks, T. C. and H. Kanamori (1979). A moment magnitude scale, *J. Geophys. Res. Solid Earth*, 84, 2348–2350.

Herrmann, R., L. Malagnini, and I. Munafò (2011). Regional moment tensors of the 2009 L'Aquila earthquake sequence, *Bull. Seism. Soc. Am.*, 101, doi:10.1785/0120100184.

Kaneko, Y. and P. M. Shearer (2015). Variability of seismic source spectra, estimated stress drop, and radiated energy, derived from cohesive zone models of symmetrical and asymmetrical circular and elliptical ruptures, *J. Geophys. Res. Solid Earth*, 120, 1053–1079, doi:10.1002/2014JB011642.

Keilis-Borok, V. (1959). On estimation of the displacement in an earthquake source and of source dimensions, *Annali di Geofisica*, 12, 205–214.

Kocharyan, G.G. (2013). Fault zone stiffness as a geomechanical factor controlling the radiation efficiency of earthquakes in the continental crust, *Dokl. Earth Sci.*, 452(1), 922–925, doi:10.1134/S1028334X13090031.

Lucente, F. P., P. De Gori, L. Margheriti, D. Piccinini, M. Di Bona, C. Chiarabba, and N. Piana Agostinetti (2010). Temporal variation of seismic velocity and anisotropy before the 2009 Mw 6.3 L'Aquila earthquake, Italy, *Geology*, 38, 1015–1018, doi:10.1130/G31463.

Malagnini, L., A. Akinci, K. Mayeda, I. Munafò, R. B. Herrmann, and A. Mercuri (2011). Characterization of earthquake-induced ground motion from the L'Aquila seismic sequence of 2009, Italy, *Geophys. J. Int.*, 184, 325–337.

Mori, J. and A. Frankel (1990). Source parameters for small events associated with the 1986 North Palm Springs, California, earthquake determined using empirical Green functions, *Bull. Seism. Soc. Am.*, 80, 278–295.

Pacor, F. et al. (2016). Spectral models for ground motion prediction in the L'Aquila region (central Italy): evidence for stress-drop dependence on magnitude and depth, *Geophys. J. Int.*, 204, 716–737.

Papadopoulos, G. A., M. Charalampakis, A. Fokaefs, and G. Minadakis (2010). Strong foreshock signal preceding the L'Aquila (Italy) earthquake (Mw 6.3) of 6 April 2009, *Nat. Hazards Earth Syst. Sci.*, 10, 19–24, doi:10.5194/nhess-10-19-2010.

Peng, Z. and Y. Ben-Zion (2006). Temporal changes of shallow seismic velocity around the Karadere-Düzce branch of the north Anatolian fault and strong ground motion, *Pure Appl. Geophys.*, 163, 567–599, doi:10.1007/s00024-005-0034-6.

Prieto, G. A., R. L. Parker, F. L. Vernon, P. M. Shearer and D. J. Thomson (2006). Uncertainties in earthquake source spectrum estimation using empirical Green's functions, in: *Earthquakes: Radiated Energy and the Physics of Faulting*, R. Abercrombie, A. McGarr, H. Kanamori, and G. Di Toro Eds., Geophys. Monogr. Ser., 170, 69–74, AGU, Washington D. C., doi:10.1029/170GM08.

Rovelli, A. and G. Calderoni (2014). Stress drops of the 1997–1998 Colfiorito, Central Italy earthquakes: hints for a common behaviour of normal faults in the Apennines, *Pure Appl. Geophys.*, 171, 2731–2746, doi: 10.1007/s00024-014-0856-1.

Rowshandel, B. (2010). Directivity Correction for the Next Generation Attenuation (NGA) Relations, *Earthquake Spectra*, 26, 525–559.

Ruhl, C. J., R. E. Abercrombie, and K. D. Smith (2017). Spatiotemporal variation of stress drop during the 2008 Mogul, Nevada, earthquake swarm, *J. Geophys. Res. Solid Earth*, 122, doi:10.1002/2017JB014601.

Savage, J. C. and M. D. Wood (1971). The relation between apparent stress and stress drop, *Bull. Seismol. Soc. Am.*, 61, 1381–1388.

Singh, S. K. and M. Ordaz (1994). Seismic energy release in Mexican subduction zone earthquakes, *Bull. Seismol. Soc. Am.*, 84, 1533–1550.

Smith, K. D. and K. F. Priestley (2000). Faulting in the 1986 Chalfant, California, sequence: local tectonics and earthquake source parameters, *Bull. Seism. Soc. Am.*, 90, 813–831.

Spudich, P. and B.S.J. Chiou (2008). Directivity in NGA earthquake ground motions: analysis using isochrone theory, *Earthquake Spectra*, 24, 279–298

Sugan, M., A. Kato, H. Miyake, S. Nakagawa, and A. Vuan (2014). The preparatory phase of the 2009 Mw 6.3 L'Aquila earthquake by improving the detection capability of low-magnitude foreshocks, *Geophys. Res. Lett.*, 41, 6137–6144, doi:10.1002/2014GL061199.

Telesca, L. (2010). A non-extensive approach in investigating the seismicity of L'Aquila area (central Italy), struck by the 6 April 2009 earthquake (ML = 5.8), *Terra Nova*, 22, 87–93, doi:10.1111/j.1365-3121.2009.00920.x.

Tsujiura, K. (1977). Spectral features of foreshocks, *Bull. Earthquake Res. Inst.*, 52, 357-371.

Uchide, T., P. M. Shearer, and K. Imanishi (2014). Stress drop variations among small earthquakes before the 2011 Tohoku-oki, Japan, earthquake and implications for the main shock, *J. Geophys. Res. Solid Earth*, 119, 7164–7174, doi:10.1002/2014JB010943.

Wang, Y. J. and K. F. Ma (2015). Investigation of the temporal change in attenuation within the ruptured fault zone of the 1999 Mw7.3 Chi-Chi, Taiwan earthquake, *Pure Appl. Geophys.*, 172, 1291-1304, doi: 10.1007/s00024-014-0854-3.

Wessel, P. and W. H. F. Smith (1991). Free Software Helps Map and Display Data, *EOS Trans., AGU*, 72 (41), 441.

Wyss, M. and J. N. Brune (1968). Seismic moment, stress, and source dimensions for earthquakes in the California-Nevada region, *J. Geophys. Res.*, 73(14), 4681-469.

Wong, T.-F. (1986). On the normal stress dependence of the shear fracture energy, in: *Earthquake Source Mechanics*, S. Das, J. Boatwright, and C. H. Scholz Eds., Geophys. Monogr. Ser., Vol. 37, 1-11, AGU, Washington, D.C,

Yoshida, K., T. Saito, Y. Urata, Y., Asano, and A. Hasegawa (2017). Temporal changes in stress drop, frictional strength, and earthquake size distribution in the 2011 Yamagata-Fukushima, NE Japan, earthquake swarm, caused by fluid migration, *J. Geophys. Res. Solid Earth*, 122, 379–10,397, doi:10.1002/2017JB014334.

Zaccarelli, L., N. M. Shapiro, L. Faenza, G. Soldati, and A. Michelini (2011). Variations of crustal elastic properties during the 2009 L'Aquila earthquake inferred from cross-correlations of ambient seismic noise, *Geophys. Res. Lett.*, 38, L24304, doi:10.1029/2011GL049750.

Zuñiga, F. R., M. Wiss, and M. E. Wilson (1987). Apparent stresses, stress drops, and amplitude ratios of earthquakes preceding and following the 1975 Hawaii Ms 7.2 main shock, *Bull. seism. Soc. Am.*, 77, 69–96.

Table 1. List of target earthquakes analyzed in this study (from 1 to 24) and EGF events (from EGF1 to EGF3). Numbers in brackets are the uncertainty intervals corresponding to the ± 1 s.d. range around the geometric mean.

N	Date (UTC)	Lat (°)	Lon (°)	Dep (km)	M _w	$\Delta\sigma$ (MPa)	τ (MPa)	η_{sw}
1	17/02/2009 06:08	42.343	13.386	8.9	2.88	0.73 (0.66–0.82)	0.10 (0.07–0.14)	0.13 (0.08–0.21)
2	17/02/2009 18:13	42.341	13.387	9.1	2.67	0.27 (0.25–0.30)	0.04 (0.03–0.06)	0.15 (0.09–0.25)
3	30/03/2009 13:38	42.337	13.392	9.4	4.08	2.06 (1.92–2.20)	0.19 (0.14–0.26)	0.09 (0.06–0.14)
4	30/03/2009 13:43	42.335	13.392	9.6	3.53	1.22 (1.13–1.32)	0.18 (0.10–0.31)	0.15 (0.08–0.28)
5	30/03/2009 17:11	42.336	13.396	9.8	2.92	0.35 (0.32–0.39)	0.04 (0.03–0.07)	0.12 (0.07–0.21)
6	30/03/2009 21:57	42.333	13.392	9.9	3.46	0.59 (0.55–0.63)	0.05 (0.04–0.07)	0.09 (0.06–0.13)
7	31/03/2009 06:04	42.327	13.393	10.0	2.74	0.40 (0.36–0.45)	0.06 (0.03–0.09)	0.14 (0.08–0.25)
8	02/04/2009 11:11	42.327	13.392	10.0	2.67	0.44 (0.39–0.49)	0.05 (0.03–0.07)	0.11 (0.07–0.18)
9	03/04/2009 06:43	42.327	13.394	10.2	2.66	0.12 (0.11–0.13)	0.03 (0.02–0.04)	0.22 (0.14–0.36)
10	05/04/2009 20:48	42.342	13.395	8.5	3.92	1.67 (1.55–1.79)	0.12 (0.08–0.16)	0.07 (0.05–0.10)
11	05/04/2009 22:39	42.342	13.402	8.4	3.47	1.26 (1.16–1.38)	0.07 (0.05–0.10)	0.06 (0.04–0.09)
12	06/04/2009 01:32	42.349	13.385	8.6	6.13	8.68 (8.07–9.34)	1.12 (0.74–1.68)	0.13 (0.08–0.21)
13	06/04/2009 06:21	42.332	13.404	8.4	3.54	0.88 (0.79–0.97)	0.06 (0.04–0.09)	0.07 (0.04–0.11)
14	06/04/2009 07:39	42.340	13.395	8.5	3.40	0.87 (0.82–0.93)	0.08 (0.06–0.11)	0.09 (0.06–0.14)
15	10/04/2009 00:36	42.335	13.400	8.5	2.89	0.76 (0.67–0.86)	0.09 (0.06–0.12)	0.11 (0.07–0.18)
16	11/04/2009 22:13	42.335	13.390	9.2	2.72	0.35 (0.32–0.38)	0.04 (0.02–0.05)	0.10 (0.07–0.16)
17	21/04/2009 15:44	42.340	13.385	9.2	3.53	0.96 (0.90–1.03)	0.11 (0.08–0.16)	0.12 (0.08–0.17)
18	02/05/2009 05:21	42.338	13.394	8.4	2.86	0.68 (0.62–0.75)	0.07 (0.05–0.09)	0.10 (0.07–0.15)
19	03/07/2009 01:14	42.337	13.380	9.7	3.48	1.54 (1.42–1.67)	0.22 (0.16–0.31)	0.14 (0.10–0.22)
20	03/07/2009 09:43	42.338	13.386	9.2	3.43	1.66 (1.54–1.79)	0.15 (0.11–0.19)	0.09 (0.06–0.13)
21	11/07/2009 18:33	42.340	13.394	8.4	2.71	0.70 (0.63–0.77)	0.09 (0.06–0.14)	0.14 (0.08–0.22)
22	12/07/2009 10:54	42.335	13.390	9.2	2.70	0.60 (0.56–0.65)	0.06 (0.04–0.08)	0.10 (0.07–0.14)
23	12/07/2009 14:11	42.340	13.391	8.7	2.83	0.61 (0.54–0.69)	0.07 (0.05–0.10)	0.12 (0.08–0.19)
24	21/07/2009 10:23	42.335	13.396	8.7	3.00	0.89 (0.81–0.98)	0.08 (0.06–0.12)	0.09 (0.06–0.13)

EGF1	06/04/2009 19:30	42.342	13.384	10.6	2.23			
EGF2	07/04/2009 01:18	42.342	13.398	9.9	2.21			
EGF3	09/05/2009 19:44	42.344	13.394	9.6	2.49			

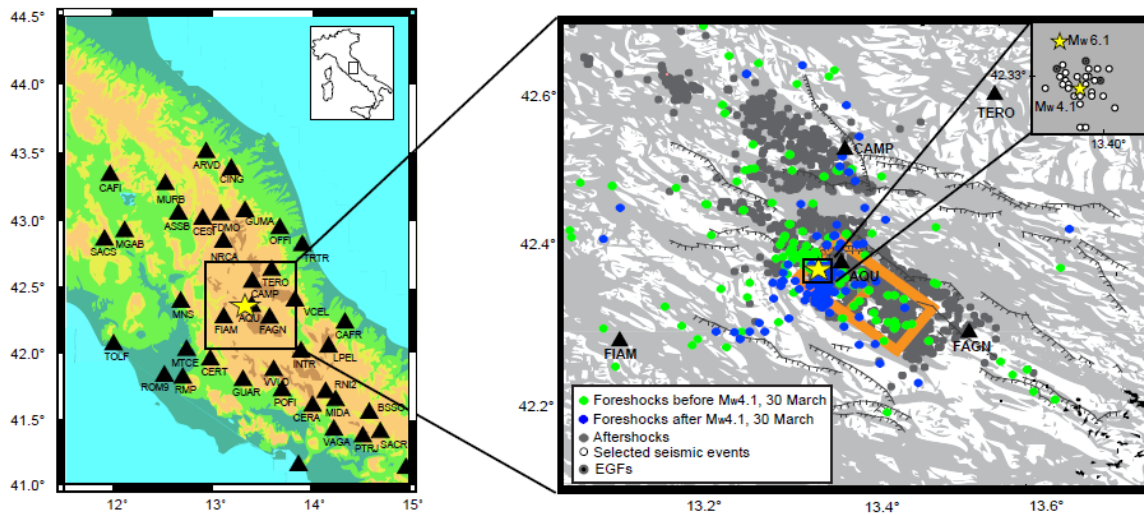


Figure 1. Map of Italy with the broad-band seismological stations used in this study (black triangles). The yellow star is the epicenter of the Mw 6.1, 6 April 2009 L'Aquila earthquake. The zoomed map shows the earthquakes of the entire 2009 seismic sequence, with many of the identified active fault traces in the region. Gray symbols are aftershocks, and green and blue symbols are foreshocks before and after the Mw 4.1 largest foreshock, respectively. This foreshock occurred one week before the main shock, and triggered a change in the seismicity rate and rock velocities in the crust. The inset is a magnified view of epicenters of the cluster under analysis, the three black dots are the EGFs.

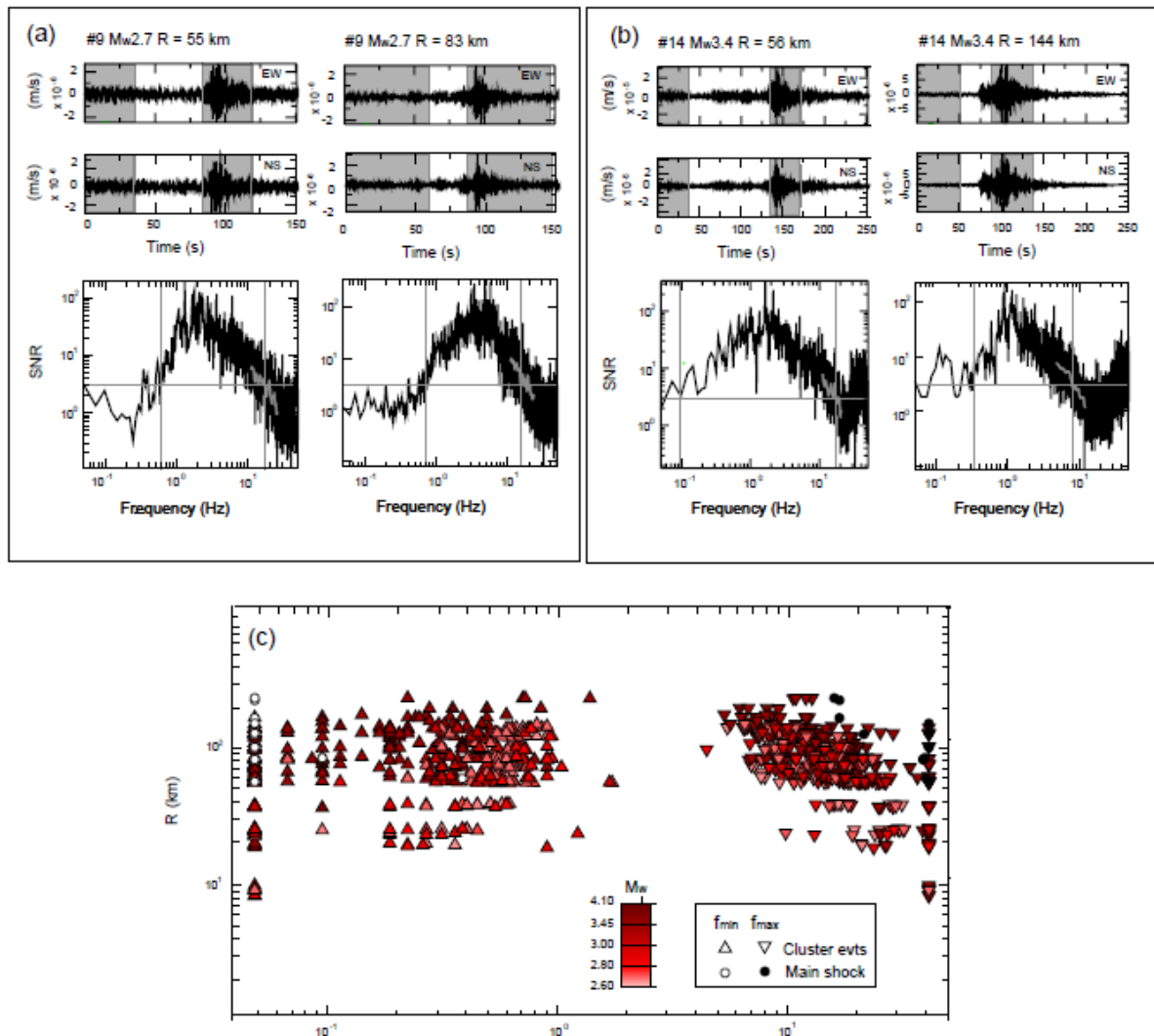


Figure 2. (a and b) Specimens of SNRs for cluster events of different magnitude. The shaded portions of the example seismograms indicate the noise and signals time windows used for the computation of the spectral ratio. The horizontal line that intercepts the SNR curve represents the threshold of 3, f_{\min} is the abscissa where SNR stably exceeds 3 at low frequency, and f_{\max} is the first abscissa where the smoothed version of the SNR curve (superimposed in grey) intercepts the threshold of 3 at high frequency. In (c), the pattern of f_{\min} and f_{\max} is shown as a function of the source distance for the entire dataset used in the analysis. The color scale varies as a function of the magnitude of the cluster events.

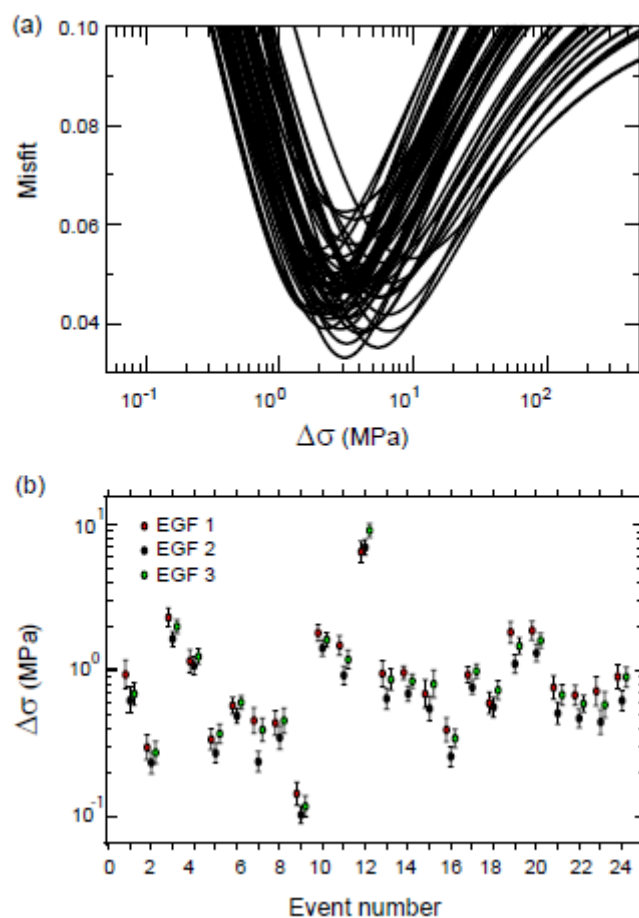


Figure 3. (a) Behavior of individual-station misfit variance for a specific event (#5 of Table 1) using the available stations of each event and three EGFs. The 5% range around the minimum is used as inverse-error weight in the average operation. (b) Comparison between the estimates of individual-event stress drop for the different EGFs.

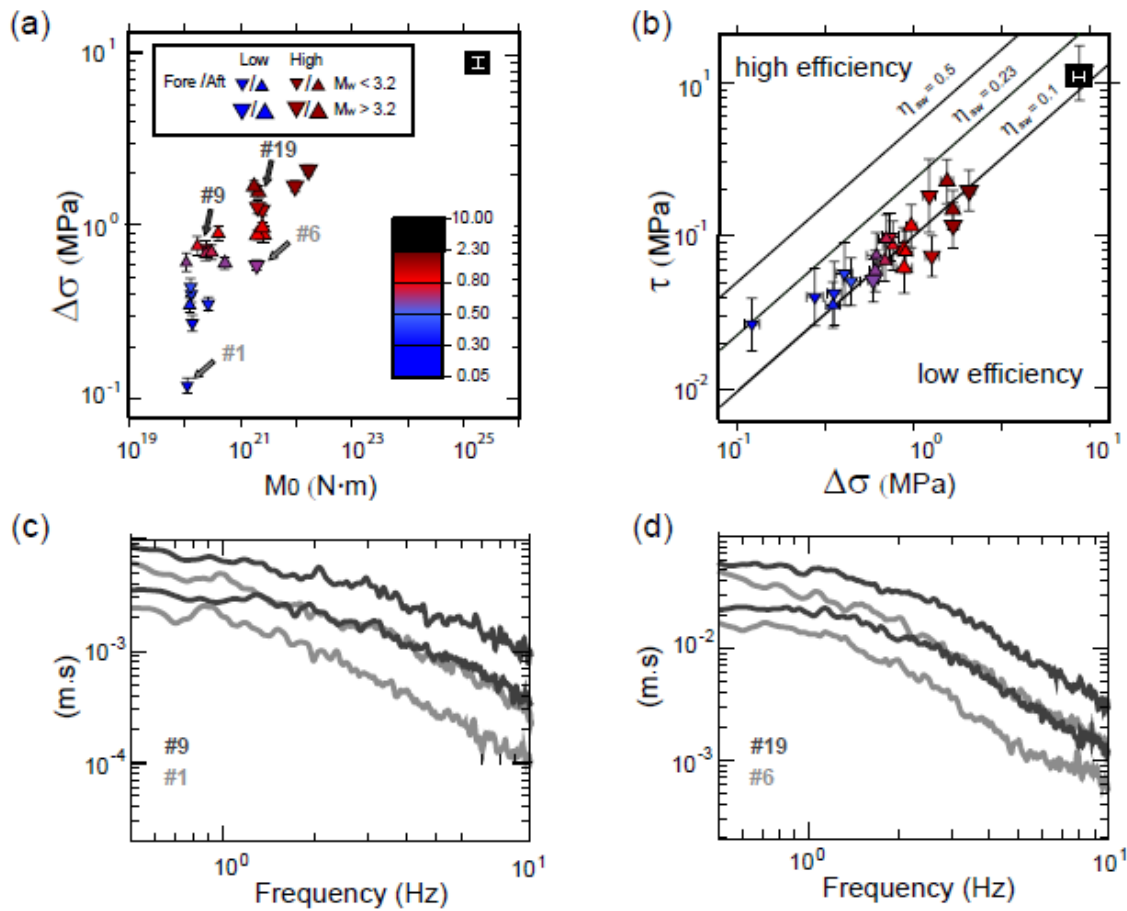


Figure 4. (a) Brune stress drop versus seismic moment. The variation of estimates of individual event is represented in a color scale with a different symbol for foreshocks and aftershocks, the triangle size depending on magnitude. Black square is the main shock. (b) Apparent stress versus Brune stress drop. The two stress parameters result in a substantial correlation, their ratio ranging mostly from 0.1 to 0.15. The straight lines with $\eta_{sw}=0.5$ and $\eta_{sw}=0.1$ represent the conventional limit for high and low efficiency ruptures, respectively, whereas $\eta_{sw}=0.23$ is the theoretical efficiency of the omega square model. (c and d) Significant differences in stress drop at similar magnitudes are confirmed by the different behavior of displacement spectra for low and high stress drop events. At low frequency there is a tight consistency because of the similar seismic moment but spectra diverge at high frequency where the ± 1 standard deviations around the mean spectrum of individual events are neatly separated. The example earthquakes of panels c and d are those indicated by the gray arrows in panel a.

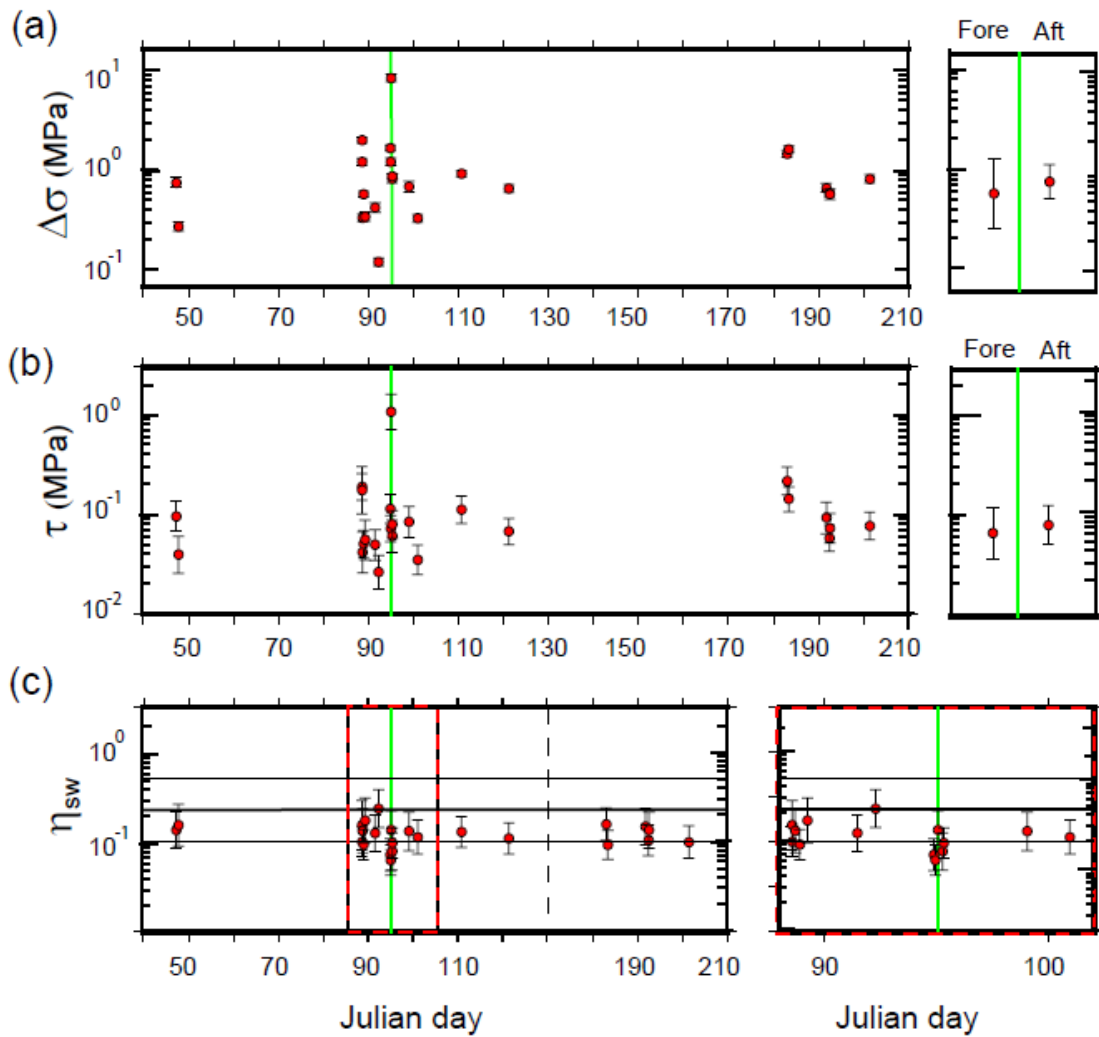


Figure 5. Behavior versus time of (a) Brune stress drop, (b) apparent stress, and (c) Savage-Wood seismic efficiency. The vertical green straight line remarks the main shock time. Panels in the right-hand side of a and b show that stress drop and apparent stress of foreshocks and aftershocks do not differ statistically. The zoomed view of Savage-Wood seismic efficiency (panel in the right hand side in the bottom row) is relative to a two-week time window, one week before and one after the main shock. Many of the smallest (< 0.1) values of η_{sw} are concentrated around the main shock time.

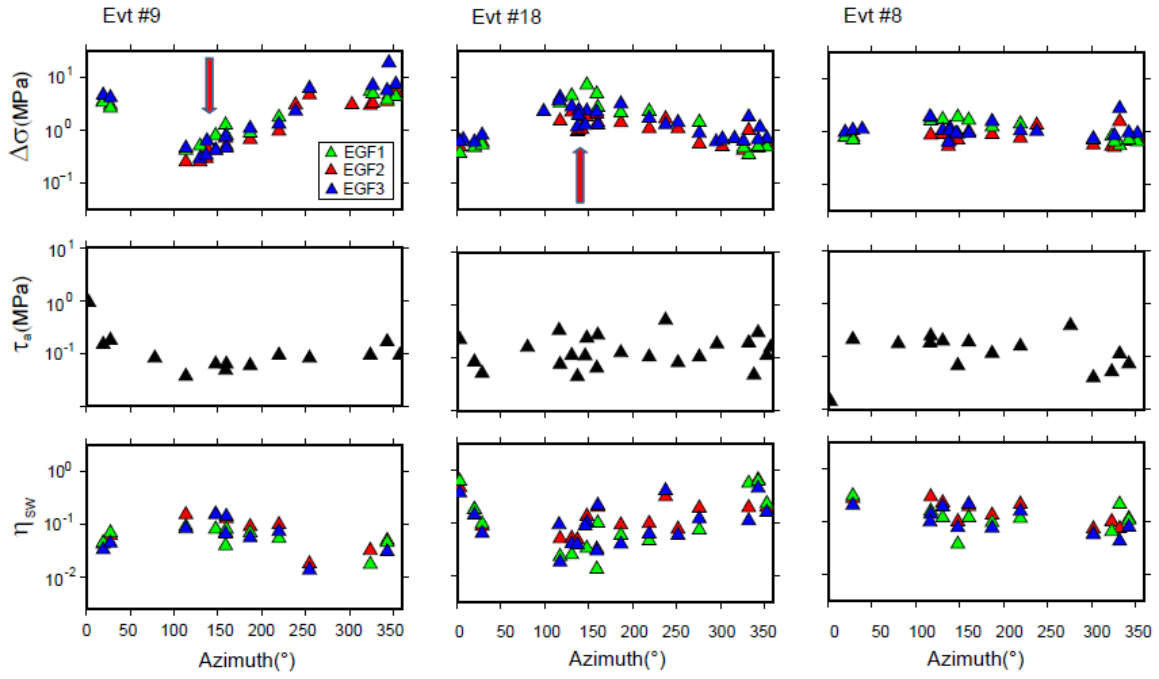


Figure 6. Azimuthal variations of the estimated source parameters. Symbols with different colors are relative to different EGFs. The red arrows indicate the L'Aquila fault strike as estimated by the *DISS Working Group* [2010].

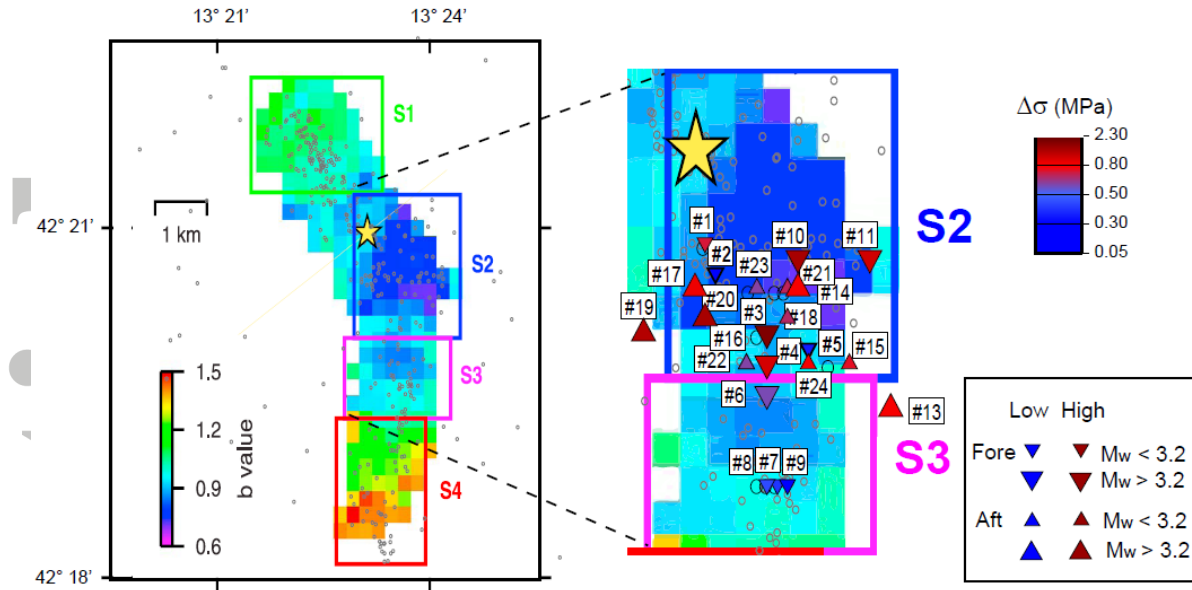


Figure 7. Zoning of b -value (redrawn from *Sugan et al. [2014]*), with the four sub-areas (S1, S2, S3, and S4, from north to south) describing the spatial variation of this parameter. The yellow star indicates the main shock epicenter. In the zoomed inset, the investigated cluster is superimposed: earthquakes fall in the sub-areas S2 (b -value 0.79 ± 0.05) and S3 (b -value 0.95 ± 0.09), their colors (from blue to red) vary according to the indicated color scale. Foreshocks and aftershocks are represented through different symbols with size depending on magnitude.

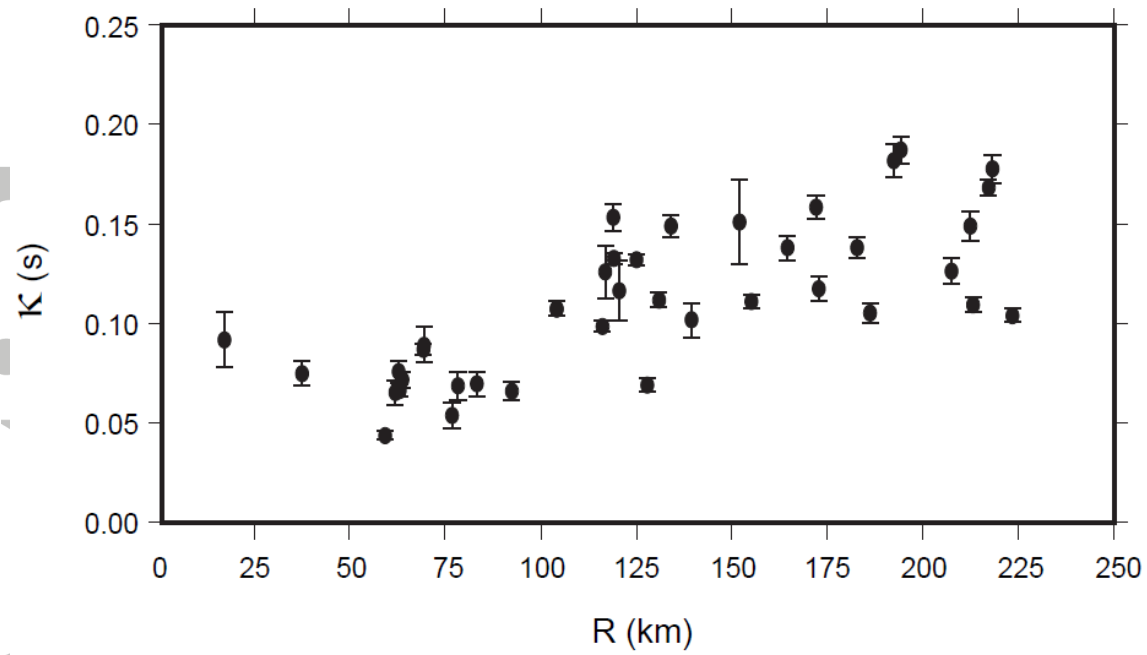


Figure A1. Estimates of κ for the stations used in the present study. The error bars are computed as the standard deviations of the mean. According to *Calderoni et al.* [2103], κ was estimated from the available records of the $M_w > 5$ earthquakes of the 2009 L'Aquila seismic sequence.

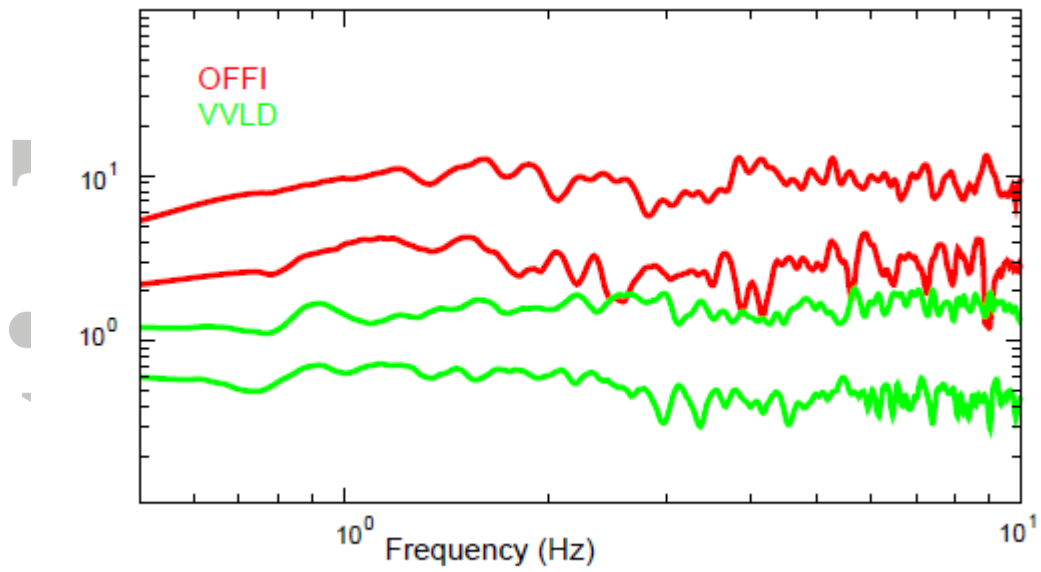


Figure A2. Site term (logarithm mean ± 1 s.d.) for two example stations characterized by significant site amplification (red) and site amplification close to 1 (green).

Accepted

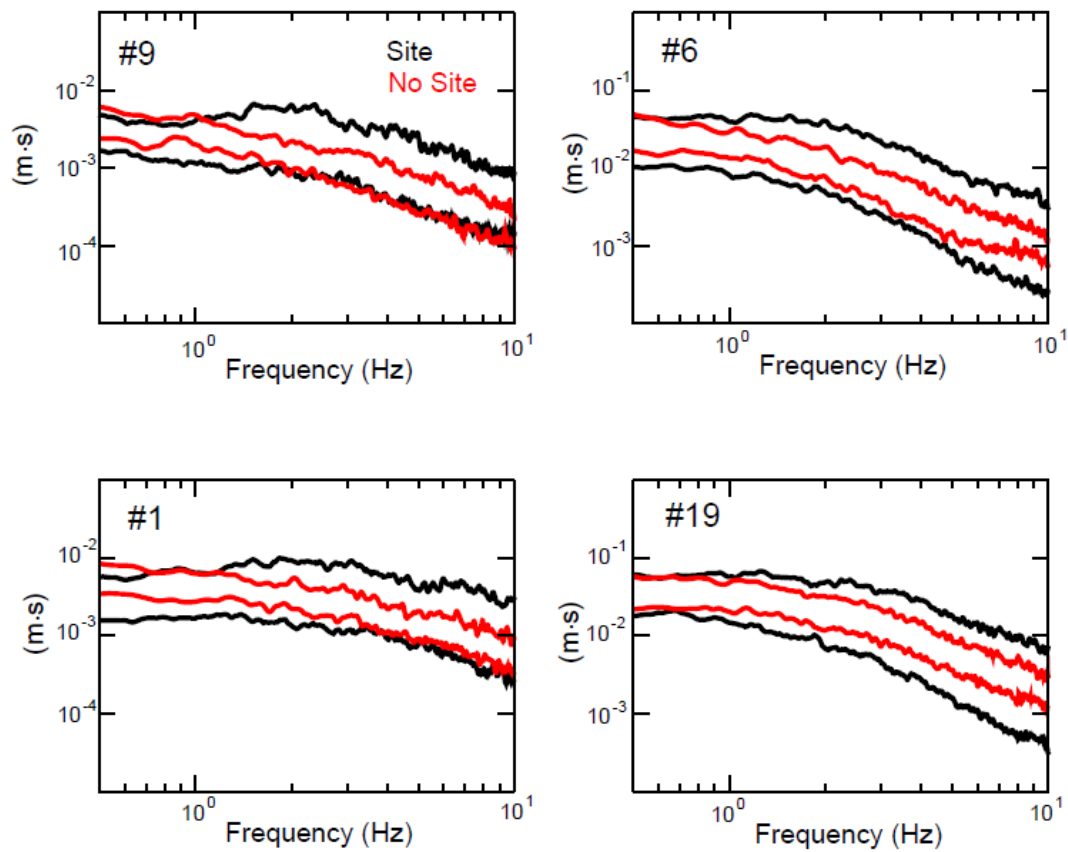


Figure A3. Comparison for some example events between the ± 1 s. d. band around the average event spectrum before (black) and after (red) the site correction. The variance after site correction is reduced by 75%, 86%, 86%, and 89% for events #9, 1, 6 and 19, respectively.

Accep

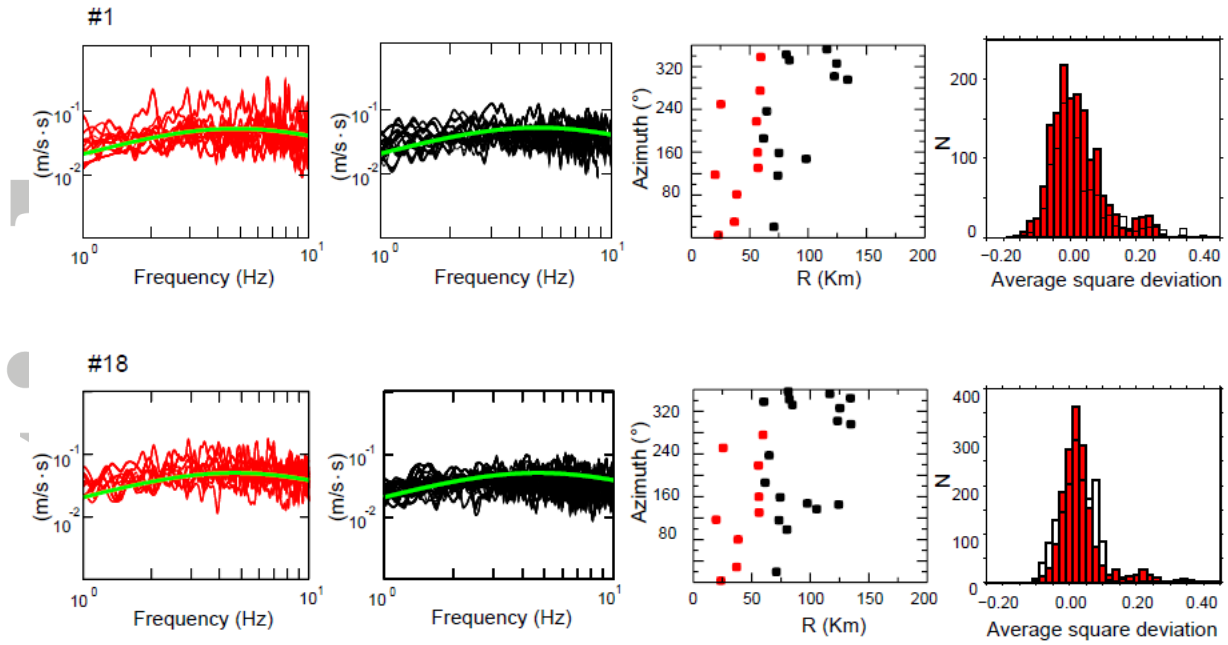


Figure A4. Check to evaluate the dispersion of individual-station spectra corrected for long-path propagation and site terms (example events # 1 and 18). Red and black curves correspond to close ($R < 60$ km) and far ($R > 60$ km) stations. Azimuth and source distance of stations available for each of the example events are shown in the third panel of each row. The theoretical Brune model (the green curve superimposed to raw data) fits satisfactorily both close and far stations. The red and black histograms represent the deviation of individual-station spectra from the theoretical source model for close and far stations, respectively. They identify two statistical populations with similar statistical properties, regardless of source distance.

Accept